Journal of Composites for Construction

Experimental study on shear behavior of reinforced concrete members fully wrapped with large rupture strain FRP composites

--Manuscript Draft--

Manuscript Number:	
Full Title:	Experimental study on shear behavior of reinforced concrete members fully wrapped with large rupture strain FRP composites
Manuscript Region of Origin:	JAPAN
Article Type:	Technical Paper
Manuscript Classifications:	188: FRP sheets; 227: Jackets; 312: RC Shear Strengthening; 344: Shear behavior of RC
Keywords:	fiber reinforced polymer (FRP); polyethylene terephthalate (PET) fiber; large rupture strain (LRS); reinforced concrete beams; shear strength; shear deformation
Abstract:	This paper presents an experimental study on the shear behavior of reinforced concrete (RC) members fully wrapped with polyethylene terephthalate (PET) fiber reinforced polymer (FRP) composites, which are a new type of FRP material characterized with a much larger rupture strain (LRS) compared to conventional FRPs (i.e., made of carbon, glass, and aramid fibers). A total of ten PET fully-wrapped RC beams, which were designed to fail in shear and with different shear-span to effective-depth ratios, transverse reinforcement ratios and shear strengthening ratios, were tested under four-point bending loads. The overall load-deflection responses and the shear deformation of the beams as well as the strain development of the transverse steel reinforcement and the FRP jackets were carefully observed. Based upon the extensive strain measurements, the shear contributions by concrete, FRP and transverse reinforcement are differentiated. It was found that the use of PET FRP composites as the jacket material of RC members can shift the mode of shear failure from a brittle one to an ideal ductile one while the ultimate state of the members is no longer caused by FRP fracture. In order to efficiently predict the shear strength of RC members wrapped by LRS FRPs, the effective strain in LRS FRPs and the degradation of concrete at the peak member shear strength must be appropriately considered.
Corresponding Author:	Tidarut Jirawattanasomkul, Ph.D. Hokkaido University Sapporo, JAPAN
Corresponding Author E-Mail:	tidarut.maintenance@gmail.com
Order of Authors:	Tidarut Jirawattanasomkul, Ph.D.
	Jian-Guo Dai, Ph.D.
	Dawei Zhang, Ph.D.
	Mineo Senda, M.Eng.
	Tamon Ueda, Ph.D.
Suggested Reviewers:	Alper Ilki, Ph.D. Professor, Istanbul Technical University, Turkey ailki@itu.edu.tr He is a leading expert in the field of seismic strengthening of RC structures. He has published several relevant papers including: Goksu, C., Polat, A., and Ilki, A. "Attempt for Seismic Retrofit of Existing Substandard RC Members under Reversed Cyclic Flexural Effects." Journal of Composites for Construction, 16(3), 286-299.
	Jian-Fei Chen, Ph.D. Professor, Queen's University Belfast, U.K j.chen@qub.ac.uk He is a leading expert in the field of FRP strengthening of RC structures and has research experience in the behavior and modeling of FRP-strengthened concrete structures. He has published several relevant papers including: Cao, S. Y., Chen, J. F.,

	Teng, J. G., Hao, Z., and Chen, J. (2005). "Debonding in RC beams shear strengthened with complete FRP wraps." Journal of Composites for Construction, 9(5), 417-428.
	Thanasis C. Triantafillou, Ph.D. Professor and Director of the Structural Materials Laboratory, University of Patras, Greece ttriant@upatras.gr He is a leading expert in the field of the application of advanced structural materials in structures, with emphasis in the field of strengthening/seismic retrofitting of RC structures. He has received “best research paper of the year” award from the ASCE of Composites for Construction (2002, 2003).
Opposed Reviewers:	
Additional Information:	
Question	**Response**
Is the article being considered for more than one journal?The Journal of Composites for Construction does not review manuscripts that are being submitted simultaneously to another organization or ASCE journal for publication.	No.
Is this article already published? Material that has been previously published cannot be considered for publication by ASCE. A manuscript that has been published in a conference proceedings may be reviewed for publication only if it has been significantly revised. If you answer YES, please provide further explanation in your cover letter.	No.
Have all the authors contributed to the study and approved the final version?All authors must have contributed to the study, seen the final draft of the manuscript, and accept responsibility for its contents. It is unethical to list someone as a coauthor who does not want to be associated with the study and who has never seen the manuscript.	Yes.
Was an earlier version of the paper previously considered and declined by ASCE?Declined manuscripts are sent through the review process again. If your manuscript has been submitted to us before under a different title, please provide that title in the space provided below. It is our policy to inform an editor that a manuscript has been previously reviewed, even when it has been reviewed by a different Division, Institute, or Council within ASCE.	No.
Do your table titles/figure captions cite other sources?If you used a figure/table from another source, written permission for print and online use must be attached in PDF format. Permission letters must state that permission is granted in both forms of media. If you used data from another source to create your own	No.

figure/table, the data is adapted and therefore obtaining permission is not required.	
Does your paper exceed 10,000 words? If YES, please provide justification in your cover letter. If you need help estimating word length, see our sizing worksheet at this link: Sizing Worksheet	Yes, I have already provided the justification in the cover letter for your kind consideration.
Estimates for color figures in the printed journal begin at $924. Cost increases depend on the number and size of figures. Do you intend for any figure to be printed in color? If YES, how many and which ones? Please provide a total count and also list them by figure number.	No.
Is this manuscript a companion to one already submitted/or being submitted? If yes, please note whether this is part I, II, or III. Please make sure all related papers are uploaded on the same day and provide the date of submission, title, and authors of each.	No.
Is this manuscript part of a Special Issue? If yes, please provide Special Issue title and name of the guest editor.	Yes, it is a Special Issue: IIFC 10th Anniversary Issue with Guest Editors: S.T. Smith and J.F. Chen.
Journal of Composites for Construction Preview is ASCE's initiative to publish author manuscripts online within 72 hours of acceptance and before the final, copyedited version of record is published in print and online. Note: Once the manuscript is posted online, it is considered published. Edits will ONLY be allowed when the corresponding author receives a proof of the composed and copyedited version of the manuscript. Your uncopyedited manuscript will be posted online unless you click the Opt-Out button below. For more information & policy: http://pubs.asce.org/journals/pap/	Opt-In (post my uncopyedited manuscript online)
To read ASCE's Data Sharing Policy, please click on the "Instructions" link associated with this question.According to this policy, you are required to report on any materials sharing restrictions in your cover letter. Are you restricted from sharing your data & materials? If yes, did you report on these in your cover letter?	No.

Submission to the Special Issue of Journal of Composites for Construction on the 10th Anniversary of IIFC

Experimental study on shear behavior of reinforced concrete members fully wrapped with large rupture strain FRP composites

Tidarut Jirawattanasomkul [(1)], Jian-Guo Dai[(2)], Dawei Zhang[(3)], Mineo Senda[(4)], Tamon Ueda[(5)]

(1) PhD Candidate, Division of Engineering and Policy for Sustainable Environment, Graduate School of Engineering, Hokkaido University, Kita 13 Jo Nishi 8 Chome Kita-ku, Sapporo, Japan, 060-8628. Email:tidarut.maintenance@gmail.com (corresponding author)

(2) Assistant Professor, Department of Civil and Environmental Engineering, The Hong Kong Polytechnic University, Hung Hom, Kowloon, Hong Kong. Email:cejgdai@polyu.edu.hk

(3) Associate Professor, Department of Civil Engineering, College of Civil Engineering and Architecture, Zhejiang University, Hangzhou, China, 310058. Email: dwzhang@zju.edu.cn

(4) Former Master Student, Division of Built Environment, Faculty of Engineering, Hokkaido University, Kita 13 Jo Nishi 8 Chome Kita-ku, Sapporo, Japan, 060-8628.

(5) Professor, Division of Engineering and Policy for Sustainable Environment, Faculty of Engineering, Hokkaido University, Kita 13 Jo Nishi 8 Chome Kita-ku, Sapporo, Japan, 060-8628. Email: ueda@eng.hokudai.ac.jp

Abstract: This paper presents an experimental study on the shear behavior of reinforced concrete (RC) members fully wrapped with polyethylene terephthalate (PET) fiber reinforced polymer (FRP) composites, which are a new type of FRP material characterized with a much larger rupture strain (LRS) compared to conventional FRPs (i.e., made of carbon, glass, and aramid fibers). A total of ten PET fully-wrapped RC beams, which were designed to fail in shear and with different shear-span to effective-depth ratios, transverse reinforcement ratios and shear strengthening ratios, were tested under four-point bending loads. The overall load-deflection responses and the shear deformation of the beams as well as the strain development of the transverse steel reinforcement and the FRP jackets were carefully observed. Based upon the extensive strain measurements, the shear contributions by concrete, FRP and transverse reinforcement are differentiated. It was found that the use of PET FRP composites as the jacket material of RC members can shift the mode of shear failure from a brittle one to an ideal ductile one while the ultimate state of the members is no longer caused by FRP fracture. In order to efficiently predict the shear strength of RC members wrapped by LRS FRPs, the effective strain in LRS FRPs and the degradation of concrete at the peak member shear strength must be appropriately considered.

Keywords: fiber reinforced polymer (FRP); polyethylene terephthalate (PET) fiber; large rupture strain (LRS); reinforced concrete beams; shear strength; shear deformation

INTRODUCTION

Many existing reinforced concrete (RC) members built using old design codes are susceptible to catastrophic collapse during a major earthquake due to their insufficient shear strength and member ductility (Priestley 1994; Priestley 2000). Use of fiber reinforced polymer (FRP) composites as the external bonding/jacketing material of RC members to improve their shear strength and ductility has been a widely used technology because of the high strength-to-weight ratio and corrosion resistance of FRP composites (Bakis et al. 2002; Karbhari and Zhao 2000). The most often used FRP composites in application include carbon fiber reinforced polymer (CFRP), glass fiber reinforced polymer (GFRP), and aramid fiber reinforced polymer (AFRP) composites, which are termed conventional FRPs in this paper. In recent years, a new category of FRP composites, which are made of polyethylene naphthalate (PEN) or polyethylene terephthalate (PET) fibers, have emerged as an alternative to conventional FRPs as the strengthening materials of RC members. These FRPs have a much larger rupture strain (LRS) (usually >5%) compared to conventional FRPs. Although their elastic modulus and strength are relatively low, they are much cheaper than conventional FRPs (Jaqin et al. 2005; Ueda 2007; Dai and Ueda 2012). It should be noted that the relatively low strength and modulus of LRS FRP can be compensated by the use of a greater amount of the fiber material whereas the small rupture strain of conventional FRP cannot be compensated in this way.

Existing tests have shown that square RC columns confined with LRS FRP composites within their plastic hinge regions can significantly improve the member ductility when subjected to cyclic lateral loading (Anggawidjaja et al. 2006; Dai et al. 2012) in the following ways: providing confinement to concrete (Dai et al. 2011; Bai et al. 2013), restraining the buckling of longitudinal reinforcement (Bai et al. 2013), and compensating the shear degradation of concrete (Anggawidjaja et al. 2006, Jirawattanasomkul et al. 2011). It is favorable that the failure mode of LRS FRP-confined RC columns subjected to lateral shear at the ultimate state is no longer governed by the brittle rupture of FRPs, which is frequently observed in conventional FRP-confined RC members and may lead to a sudden loss of the load-carrying capacity (e.g., Seible et al. 1997; Sirbu et al. 2001; Iacobucci et al. 2003)

Theoretical models have been developed to predict the compressive stress-strain relationship of LRS FRP-confined concrete under axial loading (Dai et al. 2011; Bai et al. 2013), and empirical models have been developed to predict the ductility of LRS FRP-confined RC columns under combined axial and lateral loading (Dai and Ueda 2012). However, it remains unclear how to predict the shear strength of LRS FRP-strengthened RC members, which in turn may influence the development of their flexural ductility (Jaqin et al. 2005; Jirawattanasomkul et al. 2011). The efficiency of LRS FRP composites for the shear strengthening of RC members remains a concern because concrete degradation may occur before the full activation of the strain capacity of LRS FRP composites. For instance, in the shear strengthening design of RC members using conventional FRP composites it is specified in some existing codes to limit the strain of FRP below a certain value (e.g., 0.4%), which is far below the rupture strain of LRS FRPs, to prevent possible concrete degradation (FIB 2001; JSCE 2001; ACI Committee-440 2002). Obviously, the above limitation on FRP is too conservative for LRS FRP-strengthened RC members, particularly when RC members are fully wrapped with FRP composites and the brittle debonding failure of FRP is no longer a critical concern and FRP composites can be more efficiently used. Preliminary tests have shown that RC members fully wrapped with LRS FRP composites exhibit large shear deformation and no fiber rupture when their peak shear strength is reached (Senda 2008), implying that the shear strength of LRS FRP-strengthened RC members may be reached beyond the initiation of concrete degradation. Therefore, for a good prediction of the shear strength of LRS FRP-strengthened RC members, further understanding of the efficiency of LRS FRP composites and the degradation of the concrete shear contribution is necessary.

Against the above background, this paper aims to conduct an experimental study for the first time on the shear strength and deformation behavior of RC members strengthened with LRS FRP composites. Since it is generally recommended to use LRS FRP composites as a jacketing material to confine RC columns for shear and ductility enhancement, this paper only focuses on the shear behavior of LRS FRP fully wrapped RC members.

EXPERIMENTAL PROGRAM

Details of Specimens

Ten simply-supported RC beams designed to fail in shear were subjected to four-point bending loads. RC beams rather than RC columns as the test members allows the elimination of the effects of pull-out from footings and lateral buckling of the longitudinal reinforcement, enabling more accurate shear deformation measurement. Two groups of RC beams were prepared (see Table 1):

(1) Group 1 included a reference RC beam (SP1) and five RC beams fully wrapped with different amounts of FRP composites (SP2 to SP6), all with identical longitudinal and transverse steel reinforcement as the reference beam but different strengthening ratios of FRP. Each specimen had a cross section of 250 mm × 270 mm, whose corners were chamfered with a radius of 11 mm to prevent stress concentration, and the shear span was 600 mm, resulting in a shear-span to effective-depth ratio of 2.50. The longitudinal reinforcement and transverse steel reinforcement ratios were 2.53% and 0.17%, respectively, in all the six specimens, whereas the volumetric ratio (i.e., calculated based on the nominal thickness of the LRS FRP sheets) of the wrapped LRS FRP composites varied from 0.11 % to 0.45%.

(2) Group 2 included four RC beams (SP7 to SP10) that had different sectional dimensions and shear-span to effective-depth ratios to the reference beam. This group was designed to investigate the effects of the longitudinal reinforcement ratio and shear-span to effective-depth ratio. SP7, representing a deep beam, had dimensions 250 mm × 500 mm and a shear span of 1125 mm (see Table 1), whereas SP8 and SP9 had dimensions of 250 mm × 270 mm and a shear span length of 600 mm. SP10, representing a small section of beam, had dimensions 100 mm × 150 mm and a shear span of 300 mm. The specimen corners were chamfered with a radius of 11 mm. SP7 and SP9 were designed to have a similar shear strengthening ratio and shear-span to effective-depth ratio as SP5, whereas the longitudinal reinforcement

ratio was made different. SP8 had a similar shear strengthening and longitudinal reinforcement ratio as SP3, whereas the shear-span to effective-depth ratio was made different. SP10 had a large spacing of transverse reinforcement significantly less than that required in the JSCE-2007 specification.

For all strengthened specimens (SP2 to SP10), a continuous fiber sheet with the main fibers oriented in the transverse direction was fully wrapped around the RC beam with an overlapping zone of length 250 designed to span the top side (subject to compression) of the specimens for firm anchorage.

Materials Used in the Experiments

Concrete and steel reinforcement

Two groups of specimens were cast with two batches of ready-mixed concrete with a maximum 20 mm size of aggregate. At the time of testing, the cylinder concrete strengths of the first and second batches of concrete were 25.3 MPa and 32.6 MPa, respectively. The longitudinal steel reinforcement and transverse steel reinforcement were tested to find their tensile stress-strain relationships. The longitudinal reinforcement used in the first and second groups of specimens had yield strengths 382 MPa, 360 MPa and 539 MPa (see Table 2). In specimens SP1 to SP9, the transverse reinforcement had a 6 mm diameter and a 350 MPa yield strength, whereas for SP10 the transverse reinforcement had a 13 mm diameter and the same yield strength.

LRS fiber sheets

Polyethylene terephthalate (PET) dry fiber sheets (PET-600) were used in the experiments to form LRS FRP composites. Flat coupon tests for PET FRP composites were conducted to determine their tensile properties following the JSCE standard E541-2000 (2002). The tensile coupons sheets had a nominal thickness of 0.841 mm, a length of 280 mm and a width of 13 mm. The coupon preparation followed the usual wet lay-up process involving the impregnation of a large area of fiber sheet with a matrix epoxy resin, which consisted of a main resin component and a hardener, with a mix ratio of 2:1 by weight. After one week of curing in the laboratory environment, the hardened large PET FRP plate was cut into many strips (i.e., testing coupons) with the required dimensions. Glass FRP (GFRP) tabs (25 mm long and 13 mm wide) were bonded to strengthen the two ends of each PET FRP coupon and to ensure uniform stress transfer from the loading heads during the tensile tests, which were performed at a constant loading rate equivalent to 1% strain per minute. An image measurement method was used to capture the tensile strain of each PET flat coupon with a gauge length of 45 mm (Fig. 1a). The tensile stress in the PET FRP composite was calculated from the tensile load on the basis of the nominal area of the fiber sheet. All six coupons were tested and found to fail in the central region of the specimens. Fig. 1b shows the obtained tensile stress-strain relationships, showing that PET FRP composites exhibit a bilinear stress-strain behavior caused by the motion of amorphous phases and by the sliding or failing of macromolecular chains in PET and PET fibers (Dai et al. 2011; Lechat et al. 2011). Table 3 presents a summary of the material properties of PET FRP sheets provided by the manufacturer and obtained from the present tensile tests. Two different values of elastic modulus, namely the initial elastic modulus (E_1) for the first linear portion of the stress-strain relation and the second-stage elastic modulus (E_2) for the second linear part are given in the table, together with the strain value at the transition point (ε_o) between the two linear portions.

Test Procedures and Instrumentation

All the beam specimens were tested under four-point loads and carefully instrumented during the tests to monitor the loads, mid-span beam deflections and strains of transverse reinforcement and PET FRP composites (Fig. 2a). The locations of strain gauges and LVDTs are illustrated in Figs. 2b and 2c. The strain gauges were located in the region where shear cracks are expected to occur. A network of strain gauges (with a gauge length of 10 mm) were mounted on all the transverse reinforcements at a spacing of 80 mm. Asymmetrical loading was applied to ensure failure to occur within this span. Strain gauges were also attached onto the PEF FRP at one beam side within the shear span. The gauge length was also 10 mm and the spacing between adjacent gauges was 55 mm. For each specimen, deformations were measured using LVDTs at two supports and at mid-span.

Various techniques have been attempted to measure the shear deformation of RC members, including the placement of LVDTs (e.g., Massone and Wallace 2004; Anggawidjaja et al. 2006), the use of potentiometric extensometers for curvature and shear strain measurements (e.g., Debernardi and Taliano 2006), and the laser speckle method (e.g., Ueda et al. 2002). Conventional LVDT-based methods were used here, as shown in Fig. 3a, for the measurement of shear deformation for the first batch of specimens (i.e., SP1 to SP6). However, for the second batch of specimens, the shear deformation measurement was done using a more advanced digital image correlation (DIC) method with the help of charge-coupled device (CCD) cameras (Fig. 3b). This method probes cracks and shear deformation of concrete surfaces with high image quality, low processing cost, and can monitor until the failure of specimens while avoiding causing specimen damage (Ito et al. 2002; Qi et al. 2003). For confirmation purposes, the conventional LVDT–based method was implemented in parallel with the DIC method for SP7, whereas only the DIC method was implemented for specimens SP8 to SP10 after its reliability was confirmed. The measurement of shear deformation focused on the plastic hinge region of the specimens, which is within 1.5*d* from the loading point to the support location. This region is most likely to experience shear deterioration particularly during seismic loading (Anggawidjaja et al. 2006). The frame for installing the LVDTs and the grid for the calibration points in the DIC method are shown in Figs.5a and 5b, respectively. In the DIC measurement, the measured region was divided into many square grids, each of which had four target coordinating points A, B, C and D (Fig. 5b). In order to produce a physical picture, the image was translated into the digital information of target coordinate using commercially available software such as Adobe Photoshop. Based upon the digital information, the shear deformation of each tested beam could be calculated.

RESULTS AND DISCUSSION

Failure Modes and Crack Patterns

Figure 4 shows the failure modes of specimens SP1 to SP10 presenting the sketches of the failed specimens and photographs after the removal of the LRS FRP jackets. The black lines drawn on the concrete surface show the locations of cracks, and the hatched areas indicate the bulges on the concrete surface and spalling of concrete. Except SP6, which had the largest shear strengthening ratio (Table 1), all other specimens failed in shear with clear shear deformation (i.e., no yielding of flexural reinforcement was observed before the yielding of transverse steel reinforcement). The shear failure in the ultimate state was mainly caused by the crushing of the concrete in the compression zone at the top of the critical diagonal crack (i.e., shear compression failure). At the peak load, PET FRP composites showed no sign of rupture, except in SP10. For the reference SP1, spalling of concrete cover occurred. However, in all strengthened specimens the spalling of concrete was prevented by the FRP confinement. Instead, bulging of PET FRP composites was seen at the top of the compression region, as indicated by the hatched areas in Fig. 4.

The angles of major diagonal shear cracks (θ_{cr}) were evaluated both from visible shear cracks and from the locations of maximum strains developed in transverse steel reinforcement and PET FRP sheets at different beam sections, as shown in Fig. 4 using dashed lines. The values of these angles varied from 39° to 53° to the member axis. In the first group of specimens, the reference specimen (SP1) developed two major shear cracks at an angle of 45°. In the strengthened specimens SP2 to SP5, the angle of the major shear cracks were slightly less than 45° ranging 44° to 39°. As the member deformation increased further, partial debonding of the FRP occurred near the critical shear crack or at the edge of the beam (see Fig. 5), and a loud noise was produced owing to the bulge of the concrete in the compression region. Finally, the PET FRP composites at the corner locations ruptured, leading to concrete crushing and a complete detachment of the FRP from the concrete substrate (Fig. 5). SP6, with a 0.45% volumetric ratio of FRP, showed no major shear deformation (Fig. 4) because of a confinement effect.

SP8 in the second group with a relatively high shear-span to effective-depth ratio (*a/d* =3.13) exhibited a crack angle of 49° in the plastic hinge area. In SP7, whose ratio of shear reinforcement spacing to beam depth is smaller than the others, showed the largest crack angle (θ_{cr}=53°) among all the specimens. In SP10, PET FRP sheets ruptured at the moment when the diagonal shear crack penetrated to the compression zone of concrete, and the major shear crack did not pass any transverse steel reinforcement because of their large spacing (i.e., s = 250 mm); the PET FRP sheets ruptured at the shear crack locations rather than the corners of the beam section owing to the significant shear stress transferred from the concrete to the FRP, leading to a diagonal tension failure of the member. This is an example of a poor truss mechanism by which the shear stresses were not transferred through the truss nodes, leading to member collapse in a very brittle behavior.

Overall, apart from the case when the transverse steel reinforcement ratio is extremely low, PET FRP composites prevented crack opening in the strengthened beams that leads to multiple shear cracks in the shear critical zones. Fig. 5 shows the locations where the PET FRP sheets ruptured, indicating that the breakage of PET FRP sheets usually started from the corner of the beam section near to the loading plate (e.g., in SP4). In addition, the rupture of PET FRP sheets was observed mostly at a large shear deformation level.

Overall Load-deflection Responses

The overall shear force vs. mid-span deflection responses of specimens SP1 to SP6 and SP7 to SP10 are presented in Figs. 6a and 6b, respectively; the shear force (V_t) is presented using a nominal shear stress (v_t) by dividing the shear force by the effective cross section (i.e., $v_t=V_t/bd$). The mid-span deflection is presented by the drift ratio (δ), which is defined as the ratio of the mid-span deflection (Δ_{total}) to the shear span (a).

The reference specimen (SP1) showed a linearly increasing portion until the peak load and a sudden drop of the load-carrying capacity afterwards, indicating a typical brittle shear failure of the member. During the tests of specimens SP2 to SP5 the evolution of the member's mid-span deflection was terminated at the rupture of PET FRP sheets. The corners in SP5 were not well rounded, resulting in the premature rupture of FRP at a corner, and subsequently a lower ultimate ductility was achieved compared to SP4. For SP6, which failed in flexure, neither FRP rupture nor the decrease in shear capacity was observed even at the drift ratio of 12%, at which point the test was stopped owing to the extremely large deformation. It is interesting that specimens SP2 to SP5 also exhibited significant ductility although they failed in shear. The nominal shear stress achieved in the peak of the linear portion of the load-deflection response increased with the amount of PET fiber sheets, as did the drift ratio. This is because that, with increasing strengthening ratio, the confinement provided by LRS FRP not only prevented concrete from spalling off but also restrained the widening of shear cracks. The considerable ductility development before the member's shear failure seems to be a unique characteristic of PET FRP-strengthened RC members. In other words, the shear failure is no longer brittle.

In the second group, SP10 was subjected to a brittle shear failure, and exhibited a load-deflection response similar to that of the reference SP1. The nominal shear strength of SP10 was the highest among all the specimens mainly because it had the smallest sectional dimensions (Fig. 6b). SP7 to SP9 exhibited ductile shear failure (Fig. 6b). SP7 and SP9 had similar shear-span to effective-depth ratio and strengthening ratio as SP5. The difference between these three specimens was their longitudinal reinforcement ratios; SP9, which had the lowest value, achieved the highest shear ductility, as shown in Fig. 6b, because of its highest shear to flexural strength ratio. SP7 exhibited the smallest ductility owing to its higher longitudinal reinforcement ratio, as shown in Fig. 6b. The largest sectional dimensions of SP7 may also be the reason for its lower shear ductility, because concrete degradation may be faster in the case of large-depth RC beams owing to the widening of concrete cracks in the web. This is also witnessed by the observed crack patterns (Fig. 4). SP8 had the same longitudinal reinforcement ratio and shear strengthening ratio as SP3, whereas their shear-span to effective-depth ratios were different. Both two specimens maintained a constant nominal shear stress until the drift ratio of approximately 5% (Figs. 6a and 6b). However, SP8 showed more ductility compared to SP3 because the former had a larger shear-span to effective-depth ratio than the latter (Figs. 6a and 6b).

Table 4 presents a comparison between the tested shear strengths and the predicted ones based upon existing design codes. The shear strengths are compared in terms of three components, which are from concrete (v_c), transverse steel reinforcement (v_s) and LRS FRP sheet (v_f). Each component is computed based on the existing design equations in the JSCE codes (JSCE 2001; JSCE 2007) (see Appendix). For the test values, the shear stresses carried by the transverse steel reinforcement ($v_{s\text{-test}}$) and LRS FRP ($v_{f\text{-test}}$) are obtained from their measured strain values, and then the shear contribution of concrete ($v_{c\text{-test}}$) can be obtained. The estimations of the contributions of the transverse steel reinforcement and LRS FRP also depend on the shear crack angle (θ_{cr}) of each specimen, which is also summarized in Table 4. The approaches by which the strain values of transverse steel reinforcement and LRS FRP were chosen for calculation will be elaborated later. It is seen in Table 4 that generally the shear contribution of concrete is underestimated while the shear contribution of LRS FRP composites is overestimated. The underestimation of the concrete shear contribution is due to the conservative nature of the design equations, whereas the overestimation of the FRP contribution arises because the design equation was derived from the experimental data of carbon and Aramid FRPs which often show the rupture of FRP at the peak load.

Evaluation of Shear Deformation

The shear deformation of tested beams was calculated based on Massone and Wallace's (2004) method. As shown in Fig. 7, the undeformed rectangular shape is represented by a truss element enclosed by dashed lines, whereas the deformed shape due to pure shear deformation is represented by the shaded area. The total deformation corresponding to the combined flexural and shear deformations is illustrated by the solid lines. In case of shear deformation without flexural effect, the center of rotation is located at the centroid of the truss unit. The average shear deformation (δ_s) for a specific coordinate of the concerned truss can be obtained as follows:

$$\delta_s = \frac{\sqrt{\left|d_1^{meas}\right|^2 - \left|l + u_2\right|^2} - \sqrt{\left|d_2^{meas}\right|^2 - \left|l + u_1\right|^2}}{2} - \delta_f \tag{1}$$

where d_1^{meas} and d_2^{meas} are the measured diagonal lengths of the deformed truss due to combined shear and flexural actions; u_1 and u_2 are the horizontal displacements at the top and bottom of the truss unit, respectively; and l is length of the truss unit.

The contribution of the flexural deformation (δ_f) can be attributed to the rotation of tension and compression chords, BC and AD, respectively (Fig. 7). In this study, the vertical displacements due to flexure action i.e., $\delta_{f1} = \delta_{f2} = \delta_f$ is assumed to be identical for each beam cross section and can be calculated as follows:

$$\delta_f = \alpha l \frac{u_1 - u_2}{h_1} \tag{2}$$

where: α is value describing the distance from the top of the section to the centroid of the sectional curvature distribution, and is taken as 0.5, assuming that the center of rotation is at the mid-height of the truss element; h_1 is the height of the truss unit, and l is the length of the truss unit. All the parameters used in Eqs. (1) and (2) are illustrated in Fig. 7. The values of d_1^{meas}, d_2^{meas}, u_1 and u_2 were obtained from the LVDT and DIC-based measurement methods (Figs. 3a and 3b). Shear deformation contributed to total deformation at peak load (δ_{sp}/δ_p) is also summarized in Table 4.

Figure 8 shows the relationships between the nominal shear stress (v_t) and the drift ratio due to shear deformation at the mid-span (δ_s). In the first group of specimens, SP1 shows a small value of shear drift ratio at the ultimate state. In addition, at the same loading level, its shear deformation is larger than that of other specimens, because the shear crack propagated rapidly in this reference specimen. For strengthened specimens, the shear drift ratio at the ultimate state increases significantly because PET FRP sheets restrained the widening of shear cracks, shifting the member from brittle diagonal tension failure to shear compression failure. SP6 failing in flexure shows the smallest shear drift ratio because no significant shear crack widening occurred. Therefore, the major deformation was contributed by the flexural effect. In the second group of specimens, SP7 with the greatest depth shows a significant increase in the shear deformation. SP10 failed in a very brittle manner, since all shear stresses due to concrete crack opening were transferred to FRP sheets, leading to the rupture of FRP followed by the sudden loss of the shear load-carrying capacity. The strain development in FRP sheet and transverse steel reinforcement will be reported in the next session.

Strain Development in PET FRP Sheets and Transverse Steel Reinforcement

The strains in PET FRP sheets at the shear sides of the beams in fact were induced by two types of action: (1) opening of shear cracks in concrete due to shear action, and (2) the lateral expansion of concrete in the beam section due to flexure. It is difficult to differentiate these two effects through experimental measurement. Taking SP2 as an example, Fig. 9 presents the typical strain distributions in PET FRP sheets along the shear span (Fig. 9a) as well as along the beam height (Fig. 9b) at the peak load. For each measured section (i.e., represented by a strip in Fig. 9) along the shear span, there is a maximum strain observed in the FRP sheets (Fig. 9b). Most of these maximum strains were observed around a major diagonal shear crack (see the dashed line in Fig. 9a) in the shear-critical region of the member. However, some of them deviated somewhat from the dashed lines probably due to the existence of multi-shear cracks. The high strains at the top corner of the section near the loading plate, due to the bulging of concrete, result in a dilatation of the FRP sheets in the outward direction (see Figs. 4 and 9b).

Figure 10 shows the strain distributions in transverse steel reinforcement along the shear span and the sectional depth. The strain distributions of transverse steel reinforcement in the shear-critical region are similar to those of PET FRP sheets. However, the maximum strains are always observed at the mid-height of the shear side of the beam (Fig. 10a) rather than the top corner because there is negligible effect of the concrete bulging on the transverse steel reinforcement.

The locations of strain gauges bonded on FRP sheets and transverse steel reinforcement intersected with the critical shear crack are also shown in Figs. 9 and 10. The readings of the strain gauges at these locations (i.e., marked with circles in strips F2 to F5 in Fig. 9, and in lines S1 to S3 in Fig. 10) were recorded to calculate the shear stress contribution from FRP sheets ($v_{f\text{-test}}$) and the transverse steel reinforcement ($v_{s\text{-test}}$), which represent integrals of the tensile force along each strip/line.

Figure 11 shows the typical development of the strains in transverse steel reinforcement and PET FRP sheets with the shear deformation, which is also represented by the drift ratio, until the members' ultimate states. The locations where the maximum strains in both transverse steel reinforcement and PET FRP sheets in all the specimens are summarized in Table 5 with reference to Figs. 2b, 2c and 2d. The average strains of transverse steel reinforcement and PET FRP sheets are the average values of all strain readings on the strip on which the maximum value was observed. In all the strengthened beams, the transverse steel reinforcement and PET FRP sheets tended to have similar maximum strain values before the yielding of the transverse steel reinforcement. An approximately linear increase of the maximum and average strains with the shear deformation was seen during this period. Beyond this the strain increase in transverse steel reinforcement and PET FRP sheets behaved nonlinearly. The rate of strain increase in FRP sheets and transverse steel reinforcement first increased due to the stiffness degradation of the transverse steel reinforcement and then decreased after the peak load (δ_{sp}). In the reference specimen, the increase in strain of transverse reinforcement was, however, nearly constant after the peak load because the ultimate state was reached shortly after the shear crack propagation. The strain increase in LRS FRP sheets was usually larger than that in transverse steel reinforcement because of the dual effects of LRS FRP sheets (i.e., shear strengthening and confinement effects).

The difference between the average strain and the maximum strain of FRP sheets reflects the extent of strain localization. It is seen that such a difference was smaller in SP2 (Fig. 11a) than that in SP5 (Fig. 11b). This is mainly because the location of the maximum strain observed in SP2 was closer to the major shear crack (F-18 in Table 5) while that observed in SP5 was closer to the top corner of the section. The stress concentrations at the former and latter locations tended to lead to easy debonding and fiber rupture, respectively.

Figs. 11c and 11d show the development of the maximum strain in FRP sheets and transverse steel reinforcement with the shear deformation for Group 1 and Group 2 beams, respectively. For the first group, just SP1 to SP4 are presented due to the premature failure of SP5 and the different failure mode of SP6. It is seen that the strengthening ratio influenced significantly the strain development in both FRP sheets and transverse steel reinforcement. Given the same drift ratio due to shear deformation, the higher strengthening ratio of LRS FRP sheets was used, the higher strain values developed in both the FRP sheets and the transverse steel reinforcement. For the second group of specimens, SP7 with the highest longitudinal reinforcement ratio developed higher strain values in the FRP sheets with the shear deformation compared to SP9, which had the lowest longitudinal reinforcement ratio. Strains of transverse steel reinforcement in SP9 were not available due to the breakage of gauges. Compared to all other specimens in Group 2, SP8 exhibited the faster strain development in the FRP sheets with the deflection increase during the whole loading period owing to its largest shear-span-to-effective depth ratio (a/d = 3.13).

Table 5 summarizes the maximum and average strains developed in PET FRP sheets and transverse steel reinforcement, which were observed at the peak load, the defined ultimate state (i.e., corresponding to a 20% drop of peak load), and the termination of the test. It was not possible to define the ultimate state for SP3, for which case the test was terminated before the defined ultimate state was reached, and for SP6, which exhibited no drop of the peak load. In most specimens, the strain values of the transverse reinforcement were not available at the termination of tests due to the large damage in concrete that broke the strain gauges. The maximum strains in LRS FRP sheets were usually observed at the location either close to the major shear crack or close to the one corner of the beam section. If excluding the reference SP1 and SP10, which experienced diagonal tensile shear failure, the maximum strain values in LRS FRP sheets in different states are: (1) 10,280-60,615 $\mu\varepsilon$ at the peak loads; (2) 39,756-116,613 $\mu\varepsilon$ at the defined ultimate state; and (3) 15,470-139,773 $\mu\varepsilon$ at the termination of tests; on the other hand, the maximum strain values in transverse steel reinforcement are 5,648-16,315 $\mu\varepsilon$ at the peak loads while 13,070-75,133 $\mu\varepsilon$ at the defined ultimate state. The large strain values observed in FRP sheets also demonstrate the significance of using LRS FRP sheets for maintaining the integrity and ductility of RC members at large shear deformation levels.

Degradation of the Shear Contribution of Concrete

The contribution of concrete to the shear resistance can be isolated from the total member shear force once the shear contributions of transverse steel reinforcement and LRS FRP sheets are known from the analyses on strain readings. The shear contribution of concrete in RC members wrapped with LRS FRP sheets was usually found to have reached its peak value before the full development of the member shear strength, as shown in Fig. 12. For example, in SP7 the concrete contribution to shear started degrading at the shear drift ratio of 0.80% while had degraded by 47.6% compared to its peak value at the shear drift ratio of 2.35% (Fig. 12a). A similar phenomenon was observed in all other strengthened members such as in SP10 (Fig. 12b). The extent of degradation varied from a range of 0~54.6% depending on the volumetric ratio of FRP sheets, the shear-span to effective-depth ratio and the depth of member section. Therefore, the prediction of the degradation of concrete shear contribution is essential for RC members strengthened by LRS FRP composites.

Figure 13 shows the relationships between the concrete shear stress (v_c) and the member drift ratio due to shear deformation (δ_s). In the first group of specimens, the maximum shear contributions from concrete are different for different specimens in spite of their identical sectional dimensions because the fully wrapped FRP sheets provided confinement to concrete and hence enhanced its compressive concrete strength, as shown in Fig. 13a and Table 4 ($v_{c\text{-}test}$ at peak load). In addition, the mark “×” in Figs. 13a and 13b indicates the shear drift ratio levels at which the member's shear strength was reached in SP4, SP7 to SP10 as examples. These levels (i.e., δ_{sp}) for all other specimens can be found in Table 4. In the second group of specimens, the degradation of the concrete shear contribution in SP8, which had a higher shear-span to effective-depth ratio, started earlier than that in other specimens, indicating that the shear-span to effective-depth ratio influenced the initiation of concrete degradation. In SP10, the concrete shear degradation suddenly lost after the peak due to insufficient transverse reinforcement.

The shear contribution of concrete in an RC beam depends on the stiffness of both longitudinal and transverse reinforcement (Sato et el. 1997). When the yielding of longitudinal reinforcement in tension region takes place the stiffness of this reinforcement starts to reduce, leading to the decrease of the potential shear strength of the RC beam. The yielding of longitudinal reinforcement is followed by the uplifting of the neutral axis, which limits the contribution of concrete in the compression zone. The change of neutral axis also increases the compression strain that accelerates the softening or crushing of concrete. Similarly, the yielding of transverse reinforcement also leads to its stiffness reduction and no further increase in its contribution to the member shear strength. Therefore, it is highly possible that to predict the degradation in the shear contribution of concrete in LRS FRP-strengthened RC members by correlating it to the strain levels of the longitudinal reinforcement and transverse reinforcing materials (i.e., including both FRP sheets and transverse steel reinforcement).

CONCLUSIONS

An experimental program involving tests on ten RC beams strengthened in shear with fully wrapped LRS PET FRP sheets has been conducted. The test parameters include the strengthening ratio, the longitudinal reinforcement ratio as well as the shear-span to effective-depth ratio. The following conclusions can be drawn from the test results:

(1) PET FRP sheets with a large rupture strain can be used to enhance the shear strength of RC beams while substantially increasing the member ductility. In particular, PET FRP sheets did not rupture at the peak load and led to a ductile shear failure of the strengthened RC members. This failure mode

also enabled us to clearly observe the behavior of shear strength degradation of concrete with the increase of shear deformation until the rupture of PET FRP sheets.

(2) The increase of amount of PET FRP sheets led to an increase of the shear strength and shear ductility whereas a lower longitudinal reinforcement ratio and a smaller shear-span to effective-depth ratio corresponded to improved shear ductility.

(3) PET FRP sheets developed very high strains; namely the maximum strains of 1.4-6% at the peak shear loads and as high as 15.0% at the termination of tests,.

(4) The initiation of the degradation of the shear contribution of concrete occurred even before the peak strength was developed in PET FRP-strengthened RC members. The shear contribution of concrete was found to degrade by 0-54.6% depending on the volumetric ratio of FRP sheets, the shear-span to effective-depth ratio and the member depth. This degradation of concrete contribution to shear strength is eligible in the case of no axial loading for the current study.

Due to the close relationships among the concrete shear deterioration, the member shear deformation and the strain levels in the transverse reinforcing materials including both FRP sheets and transverse steel reinforcement as observed in the current experimental study, further research work should be carried out to build up a comprehensive model to explain the above relationships. The development of such a comprehensive model is being reported by the authors and the improvement of the shear strength model by the authors (Jirawattanasomkul et al. 2011) will be reported shortly.

Acknowledgements

The authors would like to acknowledge Mr Hiroshi Nakai of Maeda Kosen Co. Ltd, Japan, for providing invaluable advice to this study and the Aramid Reinforcement Association, Japan, for providing epoxy resins and PET fiber sheets for this study. The authors are also grateful to the financial aid provided by the Grant-in-Aid for Scientific Research (A) in Japan (Project code: 22246058) and the collaboration opportunity provided by The Hong Kong Polytechnic University through the National Natural Science Foundation of China (Project code: 51172146).

Appendix: Calculation of shear contribution

According to JSCE specifications (JSCE 2001, JSCE 2007), total shear strength (v_t) consists of the contribution to shear strength due to concrete (v_c), transverse steel reinforcement (v_s) and FRP sheet (v_f).

$$v_t = v_c + v_s + v_f \tag{3}$$

The concrete and transverse steel contributions to shear strength can be calculated as follows:

$$v_c = 0.20 \cdot \sqrt[3]{f_c'} \cdot \sqrt[4]{1000/d} \cdot \sqrt[4]{100\rho_w} \tag{4}$$

$$v_s = \left[A_w f_{wy} \left(\sin\alpha_s + \cos\alpha_s\right)/s_s\right] \cdot z/\left(bd\right) \tag{5}$$

where f'_c is compressive strength of concrete; b is width of member, d is effective depth of member; ρ_w is ratio of transverse steel reinforcement; A_w is cross-sectional area of transverse steel reinforcement; f_{wy} is yielding strength of transverse reinforcement; α_s is angle of transverse steel reinforcement to the member's axis; and z is d/1.15.

The shear contribution due to FRP sheet comes from the capacity of FRP sheet to carry tensile stress from the developed strain. The nominal shear strength is computed based on the coefficient expressing the shear reinforcing efficiency of the continuous fiber sheet (K) as shown in Eq. (6). This coefficient represents the strain of FRP at breakage which varies from 0.4 to 0.8.

$$v_f = K \cdot \left[A_f f_{fu} \left(\sin\alpha_f + \cos\alpha_f\right)/s_f\right] \cdot z/\left(bd\right) \tag{6}$$

where $K = 1.68 - 0.67R$ in which $0.4 \le K \le 0.8$ and $R = \left(\rho_f E_f\right)^{1/4} \left(f_{fu}/E_f\right)^{2/3} \left(1/f_c'\right)^{1/3}$ in which $0.5 \le R \le 2.0$; A_f is cross-sectional area of continuous FRP sheets; f_{fu} is design tensile strength of continuous fiber sheet (N/mm^2); s_f is spacing of continuous FRP sheet; E_f is modulus of elasticity of continuous FRP (kN/mm^2); ρ_f is volumetric ratio of FRP sheet; and α_f is angle formed by continuous FRP sheet to the member axis.

References

ACI Committee 440. (2002). Guide for the Design and Construction of Externally Bonded FRP Systems for Strengthening Concrete Structures, American Concrete Institute, Farmington Hills, MI, USA.

Anggawidjaja, D., Ueda, T., Dai, J., and Nakai, H. (2006). "Deformation capacity of RC piers wrapped by new fiber-reinforced polymer with large fracture strain." *Cement and Concrete Composites*, 28(10), 914-927.

Bai, Y.L., Dai, J.G. and Teng, J.G. (2013). "Cyclic compressive behavior of concrete confined with large rupture strain FRP composites." *Journal of Composites for Construction*, ASCE (Accepted for publications)

Bakis, C. E., Bank, L. C., Brown, V. L., Cosenza, E., Davalos, J. F., Lesko, J. J., Machida, A., Rizkalla, S. H., and Triantafillou, T. C. (2002). "Fiber-reinforced polymer composites for construction-state-of-the-art review." *Journal of Composites for Construction*, ASCE, 6(2), 73-87.

Dai, J. G., Bai, Y.L. and Teng, J.G. (2011), "Behavior and modeling of concrete confined with FRP composites of large deformability." *Journal of Composites for Construction*, ASCE, 15(6), 963-973.

Dai, J.G., Lam, L., and Ueda, T. (2012). "Seismic retrofit of square RC columns with polyethylene terephthalate (PET) fibre reinforced polymer composites." *Construction and Building Materials*, 27(1), 206-217.

Dai, J. G. and Ueda, T. (2012). "Strength and deformability of concrete members wrapped with fibre reinforced polymer composites with a large rupture strain." *Innovative Materials and Techniques in Concrete Construction*, ISBN 978-94-007-1996-5, Edited by Fardis Michael N., Springer Publisher, Chapter 14, 225-241.

Debernardi, P. G., and Taliano, M. (2006). "Shear deformation in reinforced concrete beams with thin web." *Magazine of Concrete Research*, 58(3), 157-171.

FIB. (2001). Externally Bonded FRP Reinforcement for RC Structures, The International Federation for Structural Concrete, Lausanne, Switzerland.

Iacobucci, R. D., Sheikh, S. A., and Bayrak, O. (2003). "Retrofit of square concrete columns with carbon fiber-reinforced polymer for seismic resistance." *ACI Structural Journal*, 100(6), 785-794.

Ito, A., Aoki, Y., and Hashimoto, S. (2002). "Accurate extraction and measurement of fine cracks from concrete block surface image." *Proceeding of 28th Annual Conference of the Industrial Electronics Society*, Industrial Electronics Society, 3(1), 2202-2207.

Japan Society of Civil Engineers JSCE. (2001). "Recommendations for upgrading of concrete structures with use of continuous fiber sheets." Concrete Engineering Series Rep., Committee 292 on Concrete Structures with Externally Bonded Continuous Fiber Reinforcing Materials, Tokyo, 41.

Japan Society of Civil Engineers (JSCE). (2002). "Test method for tensile properties of continuous fiber sheets." Japan Society of Civil Engineers, JSCE-E541-2000.

Japan Society of Civil Engineers (JSCE). (2007). "Standard specification for concrete structures - structural performance verification - design." Series 2007(15), Tokyo.

Jaqin, H., Nakai, H., Ueda, T., Sato Y., and Dai, J. (2005). "Seismic retrofitting of RC piers using continuous fiber sheet with large fracturing strain." *Journal of Structural Engineering*, JSCE, 51A , 893–902.

Jirawattanasomkul, T., Ikoma, Y., Zhang D., and Ueda, T. (2011) "Shear strength of reinforced concrete members strengthened with FRP jacketing." *Proceedings of Japan Concrete Institute*, Japan Concrete Institute, 33(2), 991-996.

Karbhari, V. M., and Zhao, L. (2000). "Use of composites for 21st century civil infrastructure." *Computer Methods in Applied Mechanics and Engineerin*g, 185(2-4), 433-454.

Lechat, C., Bunsell, A. R., and Davies, P. (2011). "Tensile and creep behavior of polyethylene terephthalate and polyethylene naphthalate fibres." *J. Material Science*, 46(2), 528–533.

Massone, L. M., and Wallace, J. W. (2004). "Load-deformation responses of slender reinforced concrete walls." *ACI Structural Journal*, 101(1), 103-113.

Priestley, M. J. N., Verma, R., and Xiao, Y. (1994). “Seismic Shear Strength of Reinforced Concrete Columns.” *Journal of Structural Engineering*, ASCE, 120(8), 2310-2327.

Priestley, M. J. N. (2000). “Performance-based seismic design.” Keynote Address, *Proceeding of 12th World Conference on Earthquake Engineering*, Auckland, New Zealand, 1-22.

Qi, C., Weiss, J., and Olek, J. (2003). “Characterization of plastic shrinkage cracking in fiber reinforced concrete using image analysis and a modified Weibull function.” *Materials and Structures*, 36(6), 386-395.

Sato, Y., Ueda, T., and Kakuta, Y. (1997). “Shear strength of reinforced and prestressed concrete beams with shear reinforcement.” *Concrete Library International of JSCE*, No.29. 233-247.

Senda, M. and Ueda, T. (2008). “Experimental study on shear strengthening by continuous fiber with high fracturing strain.” *Proceedings of the Concrete Structure Scenarios*, JSMS, 8, 249-256 (in Japanese).

Sirbu, G., Ueda, T., and Kakuta, Y. (2001). “A study on shear resisting mechanism of RC columns strengthened with carbon fiber sheets.” *Journal of Structural Engineering*, JSCE, 47(3), 1289-1298.

Seible, F., Priestley, M. J. N., Hegemier, G. A., and Innamorato, D. (1997). “Seismic retrofit of RC columns with continuous carbon fiber jackets.” *Journal of Composites for Construction*, ASCE, 1(2), 52-62.

Ueda, T., Sato, Y., Ito, T., and Nishizono, K. (2002). “Shear deformation of reinforced concrete beam.” *Journal of Materials, Concrete Structures, Pavements*, JSCE, 711(56), 205-215.

Table 1 Details of test specimens

Items	unit	SP1	SP2	SP3	SP4	SP5	SP6	SP7	SP8	SP9	SP10
		Specimen									
f'_c	MPa	25.3	25.3	25.3	25.3	25.3	25.3	32.6	32.6	32.6	32.6
b	mm	250	250	250	250	250	250	250	250	250	100
h	mm	270	270	270	270	270	270	500	270	270	150
d	mm	240	240	240	240	240	240	450	240	240	120
a	mm	600	600	600	600	600	600	1125	750	600	300
a/d	-	2.50	2.50	2.50	2.50	2.50	2.50	2.50	3.13	2.50	2.50
Longitudinal reinforcement in compression		3D25 (SD345)						5D25 (SD345)	3D25 (SD345)	3D25 (SD345)	2D13 (SD360)
Longitudinal reinforcement in tension		5D25 (SD345)						10D25 (SD490)	5D25 (SD490)	4D25 (SD490)	1D25 (SD490)
Transverse reinforcement		D6	D6	D6	D6	D6	D6	D6	D6	D6	D13
ρ_{sc}	%	2.53	2.53	2.53	2.53	2.53	2.53	2.30	2.50	2.50	2.10
ρ_{st}	%	4.22	4.22	4.22	4.22	4.22	4.22	4.50	4.22	3.38	4.22
ρ_w	%	0.17	0.17	0.17	0.17	0.17	0.17	0.17	0.17	0.17	0.25
ρ_f	%	0.00	0.11	0.17	0.22	0.34	0.45	0.34	0.17	0.34	0.19
s	mm	150	150	150	150	150	150	150	150	150	250
t_f	mm	0	0.28	0.42	0.56	0.84	1.12	0.84	0.42	0.84	0.18
A_w	mm^2	63.34	63.34	63.34	63.34	63.34	63.34	63.34	63.34	63.34	253.40
E_f	GPa	0	9.58	9.58	9.58	9.58	9.58	9.58	9.58	9.58	9.58
Ew	GPa	196	196	196	196	196	196	196	196	196	196
$E_f t_f$	KN/mm	0.00	0.34	4.02	5.36	8.05	10.73	8.05	4.02	8.05	1.72
$E_w A_w/s$	KN/mm	82.76	82.76	82.76	82.76	82.76	82.76	82.76	82.76	82.76	198.67
$E_f A_f/(E_w A_w/s)$	-	-	0.03	0.05	0.06	0.10	0.13	0.10	0.05	0.10	0.01

f'_c = compressive strength of concrete cylinder; b = width of beam cross-section; h = total depth of beam cross-section; d = effective depth of beam cross-section; a = shear span; a/d = shear-span to effective-depth ratio; ρ_{sc} = ratio of compression reinforcement; ρ_{st} = ratio of tension reinforcement; ρ_w = ratio of transverse steel reinforcement; ρ_f = volumetric ratio of FRP sheet; s = spacing of transverse steel reinforcement; t_f = total nominal thickness of FRP sheet for both shear sides; A_w = total cross-sectional area of both legs for one single transverse steel reinforcement; E_f, E_w = Young's modulus of FRP sheet, and Young's modulus of transverse steel reinforcement.

Table 2 Material properties of steel reinforcement

Item	Diameter (mm)	Sectional area (mm^2)	Yielding strength (MPa)	Young's modulus (MPa)	Yielding strain (με)
Longitudinal reinforcement					
D25 (SD345)	25	506.7	382	188,000	2,000
D25 (SD490)	25	506.7	539	198,000	2,700
D13 (SD360)	13	126.7	360	180,000	2,000
Transverse Reinforcement					
D13	13	126.7	360	180,000	2,000
D6	6	31.67	350	196,000	1,800

Table 3 Material properties of PET FRP sheets

Product	Manufacturer data				Present tensile tests					
	Nominal thickness (mm)	**Tensile strength (MPa)**	**Young's modulus (MPa)**	**Rupture strain (%)**	**Nominal thickness (mm)**	**Tensile strength (MPa)**	**Strain at transition, ε_o (%)**	**Rupture strain (%)**	**E_1 (MPa)**	**E_2 (MPa)**
PET-600	0.841	740	10,000	6.7-8.2	2.5	704	0.74	6.43	21,452	9,580

Table 4 Summary of test results in shear-stress and drift-ratio component

Items		unit	Specimen									
			SP1	**SP2**	**SP3**	**SP4**	**SP5**	**SP6**	**SP7**	**SP8**	**SP9**	**SP10**
Calculation at δ_p	v_c	MPa	1.78	1.78	1.78	1.78	1.78	1.78	1.69	1.77	1.79	2.30
	v_s	MPa	1.48	1.48	1.48	1.48	1.48	1.48	1.58	1.85	1.48	1.85
	v_f	MPa	-	0.27	0.41	0.55	0.82	1.10	0.82	0.41	0.82	0.44
	v_t	MPa	3.26	3.53	3.67	3.80	4.08	4.35	4.09	4.03	4.09	4.59
	v_{mu}	MPa	5.58	5.58	5.58	5.58	5.58	5.58	5.94	5.75	6.25	6.11
	v_t/v_{mu}	-	0.58	0.63	0.66	0.68	0.73	0.78	0.69	0.70	0.65	0.75
Test at δ_p	$v_{c\text{-}test}$	MPa	1.86	2.59	2.25	2.78	2.45	2.30	1.05	0.75	1.35	4.40
	$v_{s\text{-}test}$	MPa	1.12	1.06	1.11	1.11	1.11	1.14	1.11	1.19	1.19	0.99
	$v_{f\text{-}test}$	MPa	-	0.23	0.46	0.44	0.62	1.00	1.73	1.29	1.72	0.28
	$v_{t\text{-}test}$	MPa	2.97	3.87	3.82	4.33	4.14	4.43	3.89	3.22	4.26	5.68
	δ_p	%	0.66	0.95	0.80	1.39	1.14	11.44	2.61	4.28	9.96	1.64
	δ_{sp}	%	0.48	0.23	0.16	0.42	0.22	0.91	2.35	2.70	6.13	0.62
	δ_{sp}/δ_p	-	0.73	0.24	0.20	0.30	0.19	0.08	0.90	0.63	0.62	0.38
Test at δ_u*	$v_{c\text{-}test}$	MPa	1.33	1.60	-	0.34	1.49	-	0.48	0.47	0.45	2.90
	$v_{s\text{-}test}$	MPa	1.05	1.17	-	1.22	1.08	-	1.14	1.19	1.19	1.18
	$v_{f\text{-}test}$	MPa	-	0.32	-	1.91	0.73	-	1.41	0.08	1.78	0.23
	$v_{t\text{-}test}$	MPa	2.38	3.10	-	3.46	3.30	-	3.03	2.58	3.42	4.31
	δ_u	%	0.96	3.76	-	8.46	4.06	-	6.60	5.28	12.06	2.49
At the end of test	$v_{c\text{-}test}$	MPa	1.25	1.30	1.17	0.00	0.99	2.30	0.12	0.35	0.00	0.00
	$v_{s\text{-}test}$	MPa	1.11	1.11	1.17	1.22	1.08	1.14	1.13	0.80	1.19	1.88
	$v_{f\text{-}test}$	MPa	0.00	0.13	1.15	0.80	0.38	1.00	0.21	0.29	1.55	0.22
	$v_{t\text{-}test}$	MPa	2.37	2.54	3.49	2.01	2.45	4.43	1.46	1.44	2.61	1.79
	δ_{end}	%	1.07	4.89	5.27	11.42	6.0	11.44	8.84	9.53	13.05	8.59
Major shear crack angle (θ_{cr})		-	45°	44°	39°	39°	39°	N.A	53°	49°	46°	45°
Failure mode		-	Shear. comp	Shear. comp	Shear. comp	Shear. comp	Shear. comp	Shear. comp	Shear. comp	Shear. comp	Flexure	Diag. tens

*The ultimate state (δ_u) is defined to be reached with the load dropped by 20% compared to its peak load; Shear. comp = Shear compression failure; Diag. tens = Diagonal tension failure.

Table 5 Strain development in PET FRP sheets and transverse steel reinforcement

State	Specimen		SP1	SP2	SP3	SP4	SP5	SP6	SP7	SP8	SP9	SP10
At peak load (δ_p)	**FRP strain (ε_f)**	**Recorded location**	-	F-18	F-18	F-18	F-17	F-18	F-39	F-25	F-16	F-4
		Max	-	14,612	17,450	19,370	12,830	10,280	46,340	60,615	38,970	11,040
		Average	-	10,671	12,119	13,532	6,522	6,496	5,498	14,837	27,109	4,120
	Transverse steel reinforcement strain (ε_w)	**Recorded location**	S-3	S-8	S-8	S-8	S-8	S-5	S-6	S-12	N.A	S-2
		Max	15,200	10,355	17,276	16,315	13,145	13,817	15,618	31,650	N.A	673
		Average	5,648	7,262	9,424	13,651	8,920	13,062	15,618	24,182	N.A	581
At ultimate state (δ_u)	**FRP strain (ε_f)**	**Recorded location**	-	F-18	F-18	F-18	F-17	F-18	F-39	F-25	F-16	F-4
		Max	-	45,450	-	135,719	39,756	-	116,613	73,064	49,210	7,680
		Average	-	39,450	-	108,575	11,213	-	42,332	43,770	27,913	2,693
	Transverse steel reinforcement strain (ε_w)	**Recorded location**	S-3	S-8	S-8	S-8	S-8	S-5	S-6	S-12	N.A	S-2
		Max	15,192	29,306	-	75,133	31,029	-	13,071	38,968	N.A	829
		Average	5,635	20,816	-	75,133	16,021	-	11,571	33,119	N.A	476
At the end of test	**Maximum strain in FRP**		-	58,198 (F-14)	129,616 (F-18)	99,779 (F-18)	48,783 (F-17)	15,470 (F-16)	139,773 (F-39)	147,773 (F-25)	53,231 (F-16)	6,160 (F-4)
	Maximum strain in transverse steel		15,464 (S-3)	36,711 (S-8)	N.A	N.A	N.A	N.A	N.A	N.A	N.A	1,261 (S-2)

*N.A Not available owing to strain gauge breakage

Figure
Click here to download Figure: 20130422Figures.docx

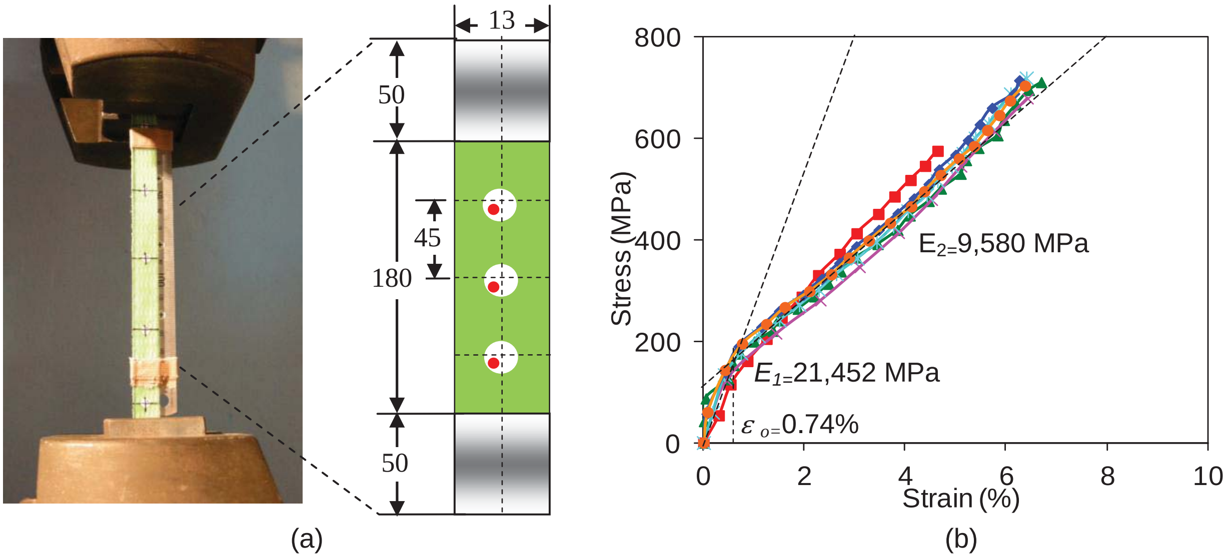

Fig. 1 Tensile test of flat coupon: (a) Tensile test and flat coupon; and (b) Stress-strain relationship of flat coupon

(a)

(b)

(c)

(d)

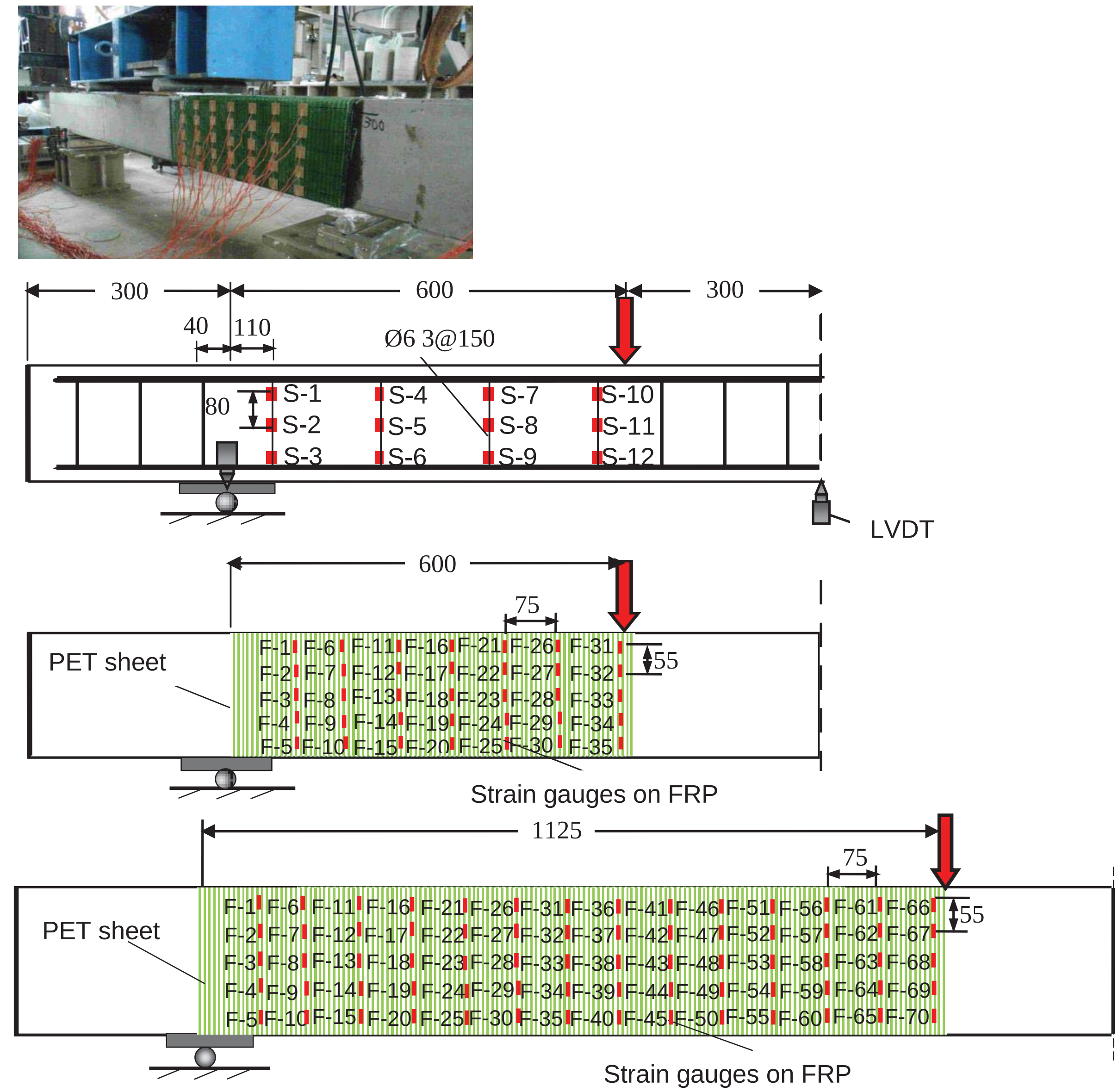

Fig. 2 Test setup: (a) asymmetrical loading; (b) locations of strain gauges on steel reinforcement; (c) locations of strain gauges on FRP (SP1-SP6, SP9); (d) locations of strain gauges on FRP (SP7)

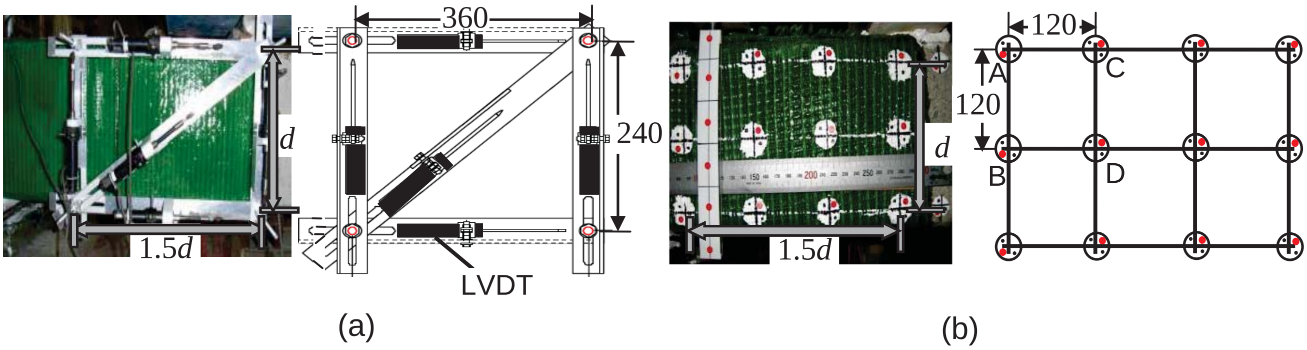

Fig. 3 Measurement of shear deformation: (a) Strain deformation measurement using LVDTs in SP1 to SP6; and (b) strain deformation measurement using image analysis in SP7 to SP10

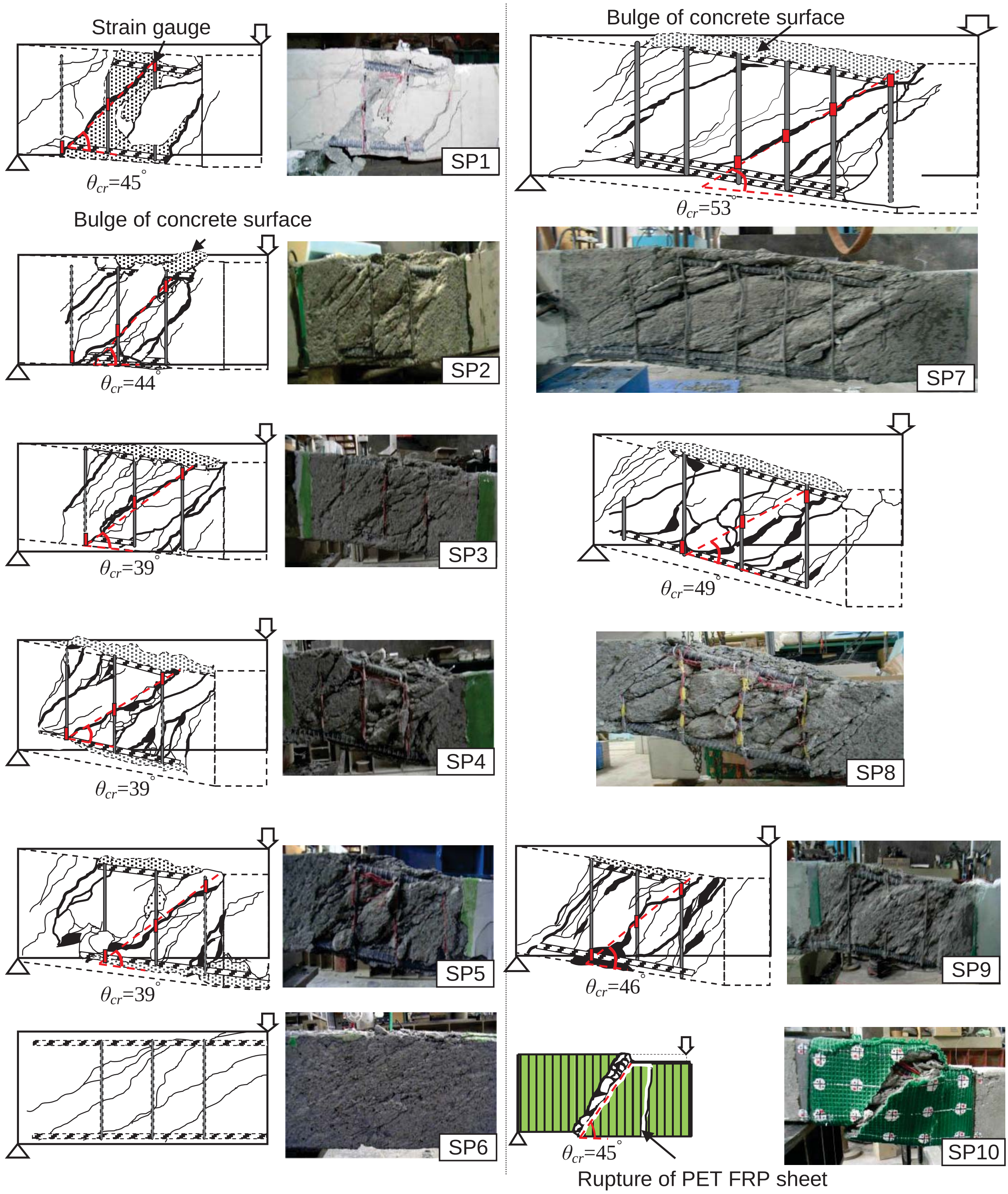

Fig. 4 Failure modes and crack patterns

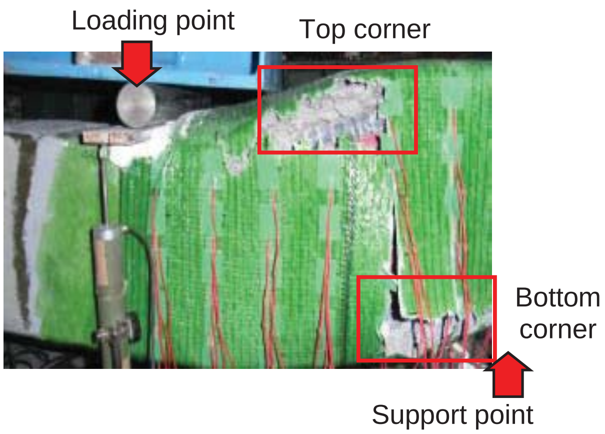

Fig. 5 Rupture and debonding location in PET sheet at termination of test in SP4

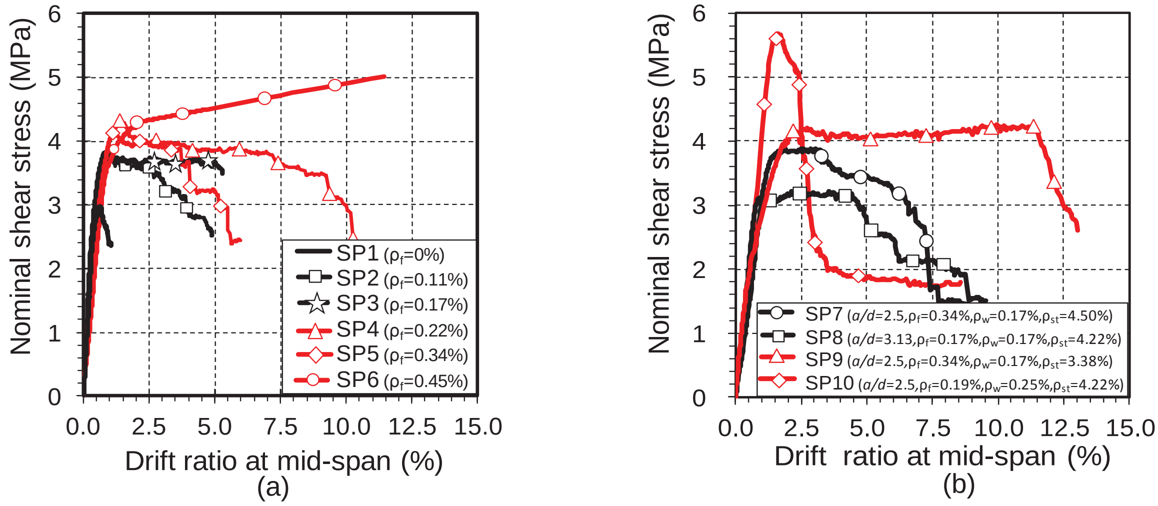

Fig. 6 Relationships between nominal shear stress (v) and drift ratio at mid-span (δ): (a) SP1 to SP6; and (b) SP7 to SP10

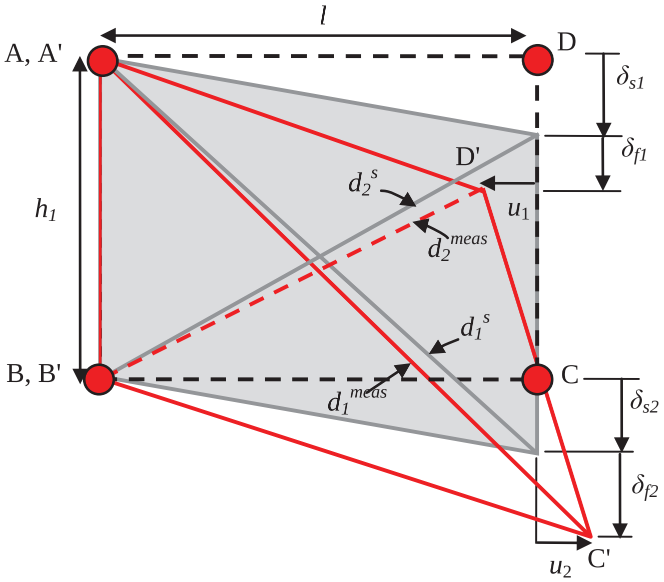

Fig. 7 Deformed configuration (Massone and Wallace 2004)

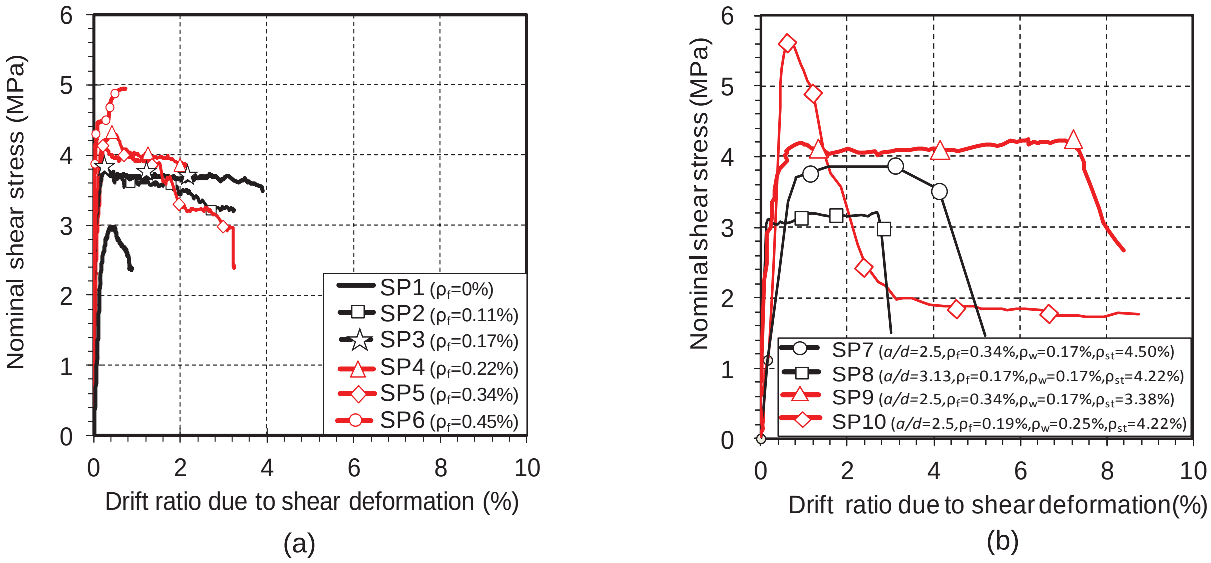

Fig. 8 Relationships between nominal shear stress (v_t) and drift ratio due to shear deformation at mid-span (δ_s): (a) SP1 to SP5; and (b) SP7 to SP10

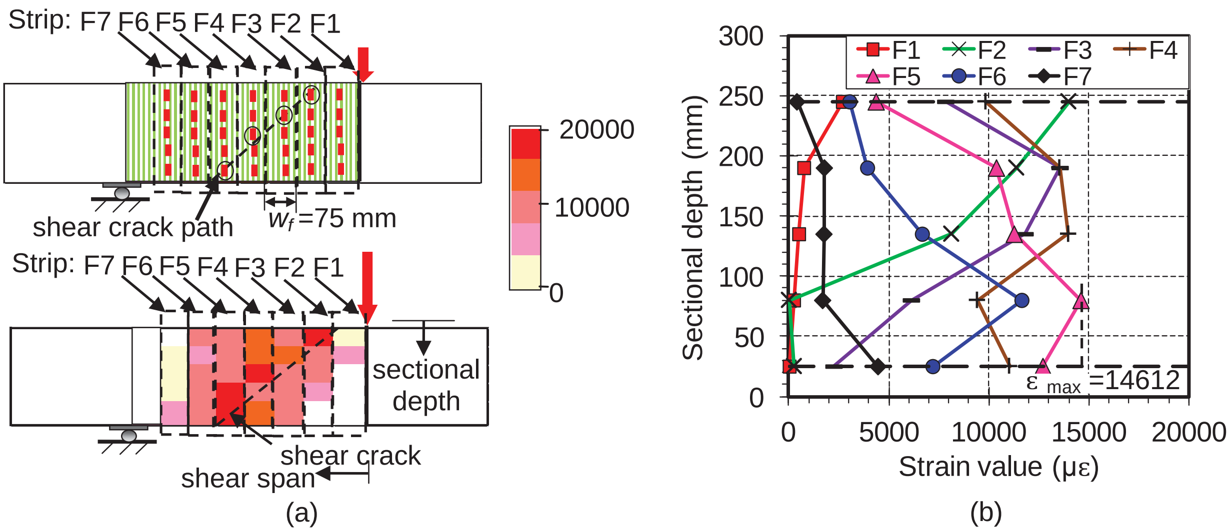

Fig. 9 Strain distribution of PET FRP sheet along the shear-span length at peak load: (a) strain of SP2 along shear-span; and (b) strain of SP2 along sectional depth

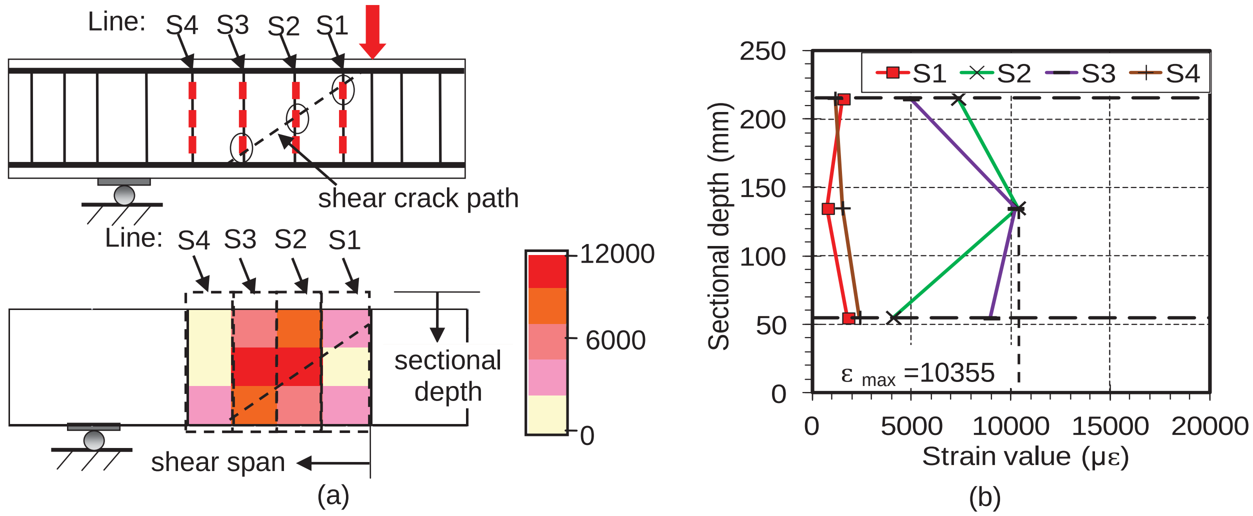

Fig. 10 Strain distribution of transverse steel reinforcement s along the shear-span length at peak load: (a) strain of SP2 along shear-span; and (b) strain of SP2 along sectional depth

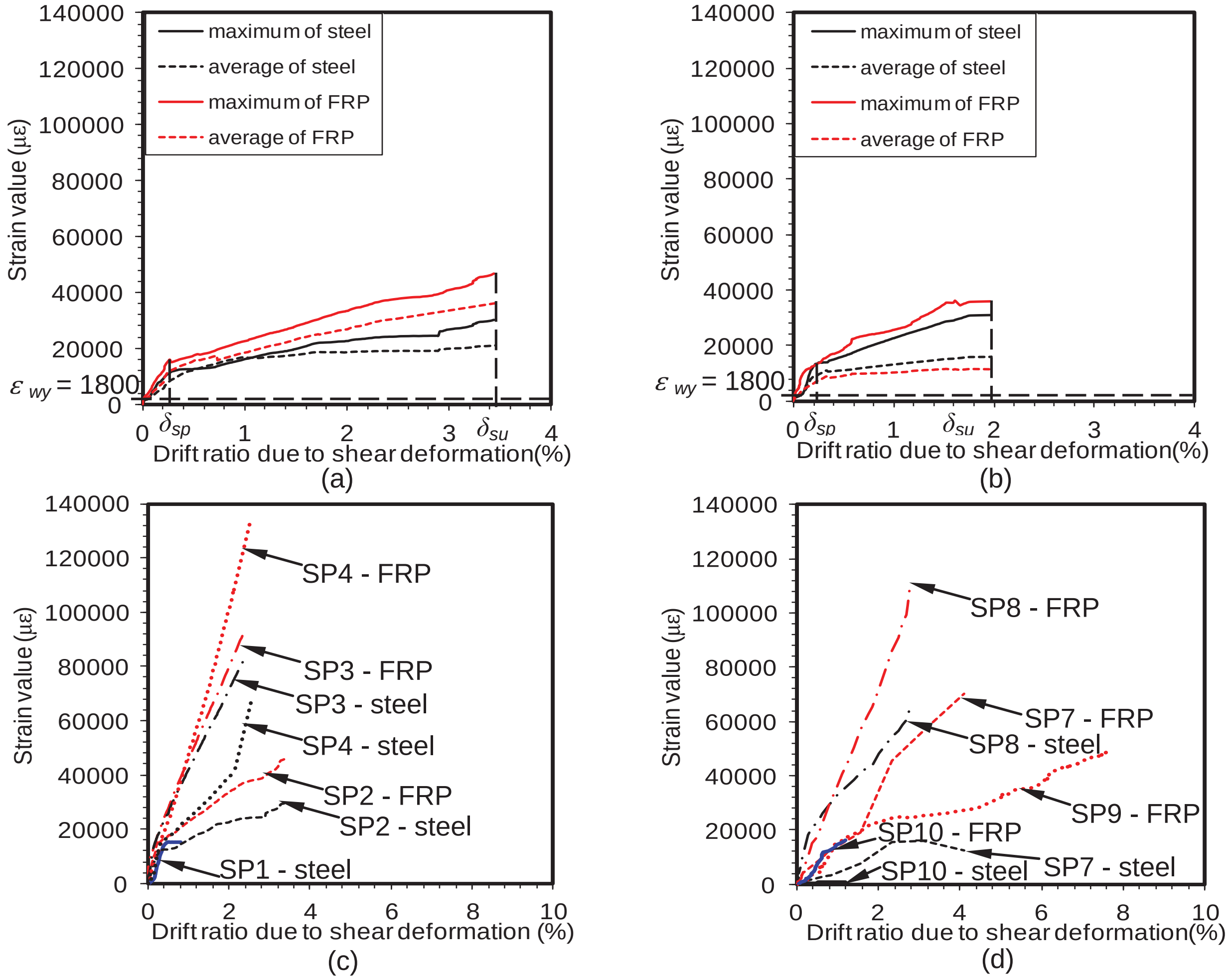

Fig. 11 Strain development of PET FRP sheet and steel reinforcement until ultimate deformation: (a) SP2; (b) SP5; (c) SP1 to SP4; and (d) SP7 to SP10

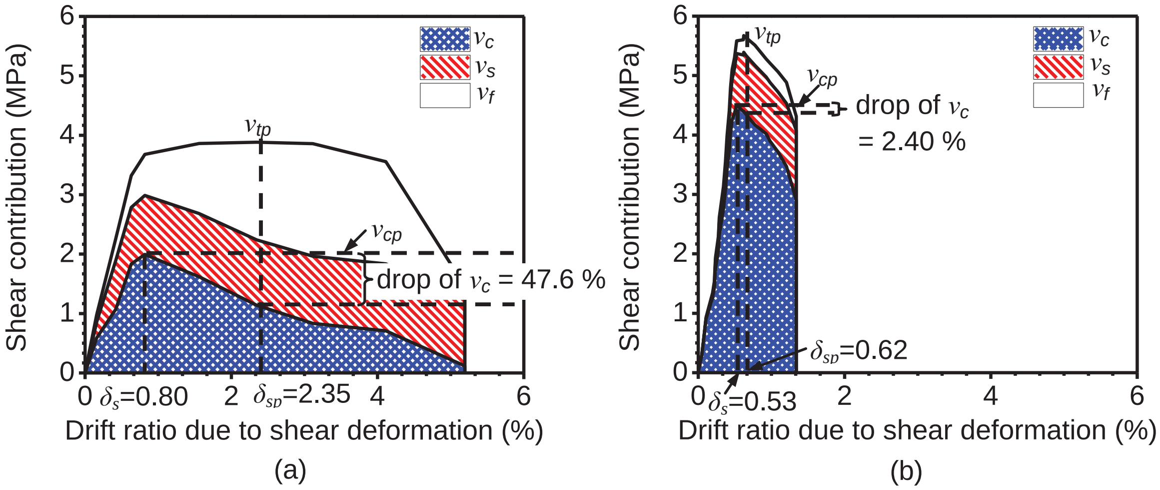

Fig. 12 Component of shear contribution: (a) SP7; and (b) SP10

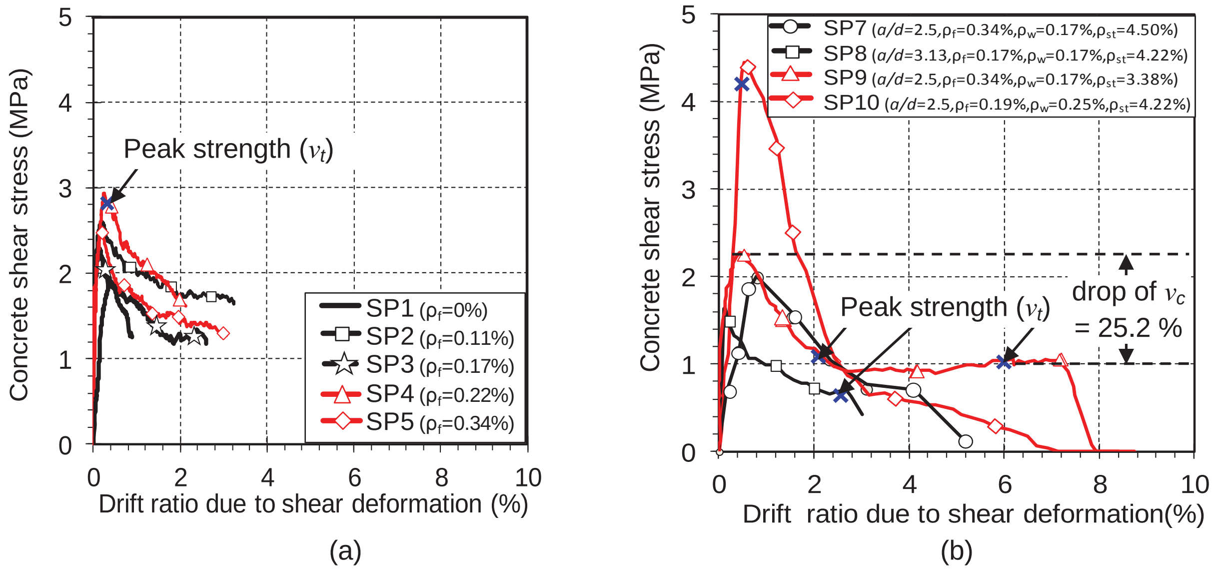

Fig. 13 Relationships between concrete shear stress (v_c) and drift ratio due to shear deformation at mid-span (δ_s): (a) SP1 to SP5; and (b) SP7 to SP10

List of Table Captions:

List of figure captions:

Fig. 12 Component of shear contribution: (a) SP7; and (b) SP10

Fig. 13 Relationships between concrete shear stress (v_c) and drift ratio due to shear deformation at mid-span (δ_s): (a) SP1 to SP5; and (b) SP7 to SP10